UNIVERSITY OF BRISTOL

University of Bristol - Explore Bristol Research
General rights

Contents lists available at ScienceDirect

Materials & Design
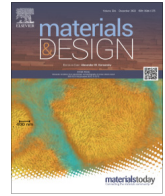
Design space and manufacturing of programmable 4D printed continuous flax fibre polylactic acid composite hygromorphs

Charles de Kergariou [a],*, Antoine Le Duigou [c], Adam Perriman [b], Fabrizio Scarpa [a]

[a] Bristol Composites Institute, School of Civil, Aerospace and Mechanical Engineering, University of Bristol, University Walk, Bristol BS8 1TR, UK
[b] School of Cellular and Molecular Medicine, University of Bristol, University Walk, Bristol BS8 1TD, UK
[c] University Bretagne Sud, IRDL, Polymer and Composites, UMR CNRS 6027, 56100 Lorient, France

HIGHLIGHTS

- Design space of 4D printed flax/ PLA hygromorphsvia printing path tailoring.
- Calla lily-inspired actuator printed, and performance assessed via DIC.
- Actuation amplitude and authority controlled via tilting and bending of filamentss.
- Comparison of experiments and analytical/numerical models for hygromorphs performed.

GRAPHICAL ABSTRACT
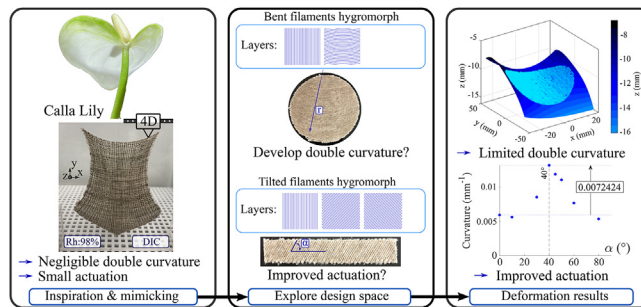
ARTICLE INFO

ABSTRACT

The work describes the exploration of the design space by fabrication, modelling and testing of bio-based and humidity-triggered 4D printed shape-changing biocomposites. The aim is to broaden the understanding of the control actuation via printing path tailoring and unlock new potential applications for biomaterials and autonomous actuator design. The composites are made with continuous flax yarns and polylactic acid matrix filaments and exhibit moisture-induced actuation. The actuation capability is first demonstrated by printing a calla lily flower-inspired configuration subjected to 98% relative humidity. This structure did not however achieve the anticlastic double curvature and large actuation targeted. To resolve these issues, cross-ply composite architectures with bent filaments deposited in one layer have then been developed. The amplitude for curvature control ranges obtained were $1.9*10^{-3}$mm^{-1} and $7.9*10^{-3}$mm^{-1} depending on the position on the specimen. Other cross-ply hygromorphs solutions are also proposed, with the orientation of their passive layers ($[0°]_2$) tilted by α degrees (stacking sequence: $[-\alpha, \alpha, 90°]$). The largest actuation curvature was obtained when $\alpha=40°$, which increased by 0.0072 mm^{-1} when compared to $\alpha = 0°$. The hygromorphs presented in this work are modelled using in an in–house filament scale finite element model able to capture the complexity of the printed hygromorphs architectures.

1. Introduction

Self-folding actuators are structures capable of providing actuation authority in response to an environmental change, like a variation of temperature or humidity [1]. Structures that are moisture actuated are called hygromorphs. Potential applications of these shape-morphing structures include sun orientation trackers [2] and humidity self monitoring buildings [3]. Composites are often described as efficient materials for developing shape-morphing capabilities [4,5]. The actuation for hygromorphs biocomposites (HBCs) can be triggered either by the moisture-induced expansion

---

* Corresponding author.
  E-mail address: charles.dekergariou@bristol.ac.uk (C. de Kergariou).

of the matrix [4] or the fibres [6]. Due to their high hygroscopic expansion, natural fibres are of prime interest to hygromorphs [7]. Most natural fibres are hydrophilic due to their hemicellulose and pectin content. Pectin molecules favours hydrogen bonding with water. Upon uptake of water, the hygroscopic expansion of the fibres is responsible for the deformation of the matrix and the actuation of the HBCs [8]. Despite their sensitivity to moisture degradation, flax fibres are often used in hygromorph biocomposites because their stiffness is similar to the one of glass fibres and their worldwide availability [9,10]. Moreover, the use of thermoplastic polylactic acid (PLA) as matrix adds a further element of environmental sustainability, as the overall composite can be recycled through re-melting and is biodegradable. Modern 3D printers allow the production of the complex geometries that hygromorph require. For instance, Gladman et al. have mimicked the geometry of plants (among others, calla lily flower) by 3D printing cellulose fibril reinforced hydrogels [11]. Although short fibres (e.i. fibrils) composites allow for greater flexibility to print complex geometries, they lack load-bearing capabilities compared to their continuous fibre counterparts [12,13]. The development of materials that exhibit both hygromorphic actuation and load-bearing capabilities would provide new design spaces for multifunctional adaptive composites. To the authors' knowledge, no extensive exploration of the design space for 3D printed continuous flax fibre reinforced PLA hygromorphs has been so far described in open literature. Nature provides a source of inspiration for developing actuators [14]. The pine cone has inspired several examples of hygromorph structures [15,16]. Artificial fish swim bladders from hygromorphic hydrogels and PLA scaffolds have shown some interesting actuation authority and speed control capabilities [17]. The 4D printing technique has also the potential to produce bioinspired structures, as it can take advantage of environmental stimuli to actuate a printed structure in a predictable manner [18–20]. The 4D printing techniques can be used to reproduce complex structures mimicking carnivorous plants. For example, Poppinga et al. have described the deformation via buckling present in *Aldrovanda vesiculosa* and *Dionaea muscipula* [21]. The mimicking of such structures has already been tried with different materials [22,23]. To the best of the authors' knowledge, no artificial bio mimicking 4D print has been however made so far by using continuous fibre composite actuators.

Analytical Timoshenko beam-based calculations are often used to explore the design space of 1D slender actuator beams, with layer thicknesses and stiffness as variables [3,15]. The design space of bi-material hygromorphs and their actuation process have been previously explored by mapping the distribution of the two materials in the structure using Finite Elements Analysis (FEA) [17,24]. FE models were also implemented at layer scale to explore the design space of shape memory polymers [25,26]. The design of the stacking sequence in composite actuators is made possible by implementing classical laminate theory (CLT) [27]. The previously mentioned composite structures designed using CLT, Timoshenko and FEA techniques had either an isotropic bi-material configuration, or composite properties homogenised at ply scale. A model at deposited filament scale is, however, needed to explore the 4D printing design space. Gladman et al. developed an analytical approach that provides a bridge between the equations describing the surface curvatures and the printing streamlines [11]. The design optimisation of actuators can also be inspired by strength and stiffness optimisation tools. For instance, Kubalak et al. were able to optimise the material orientation of their truss structure for the best compliance to a specific load bearing problem [28]. Those authors were also able to develop the discontinuous printing path from the material orientation obtained after optimisation [29]. A modelling technique capable of reproducing, optimising and designing structures with complex and continuous filament

paths has been previously reported [30]. The development of this technique, allows to observe the impact of the printing artefacts on the actuation, like the u-turns defined in [13]. Also, no previous comparison on how all the models used to represent the hygromorphic actuation has been discussed in open literature as yet.

The first aim of the present work is related to the possibility of mimicking the shape of a calla lily flower by a 4D printed biobased composite structure via humidity-triggered actuation. The second objective is to highlight the limitations of the actuation in complex plant-like hygromorphs structures observed during experiments. A third objective is to show how to increase the responsiveness (i.e., the amplitude) of the actuation of hygromorphs by tilting the passive layers of a classic cross ply stacking sequences ([0°;0°;90°]), to create composites with ply orientation of the type [-α°;α°;90°]. In the present work the authors aim to obtaining a double curvature space for the hygromorphs by bending the printed filament of the passive layer in a cross-ply configuration. The responsiveness was also controlled by bending the printed filament of cross ply stacking sequence. As a final objective, the work aims at assessing the efficiency of models like the Timoshenko bilayer, shell/solid and in house finite elements to design bio-based hygromorph 4D printed composites. The voxel-based model is an in–house developed technique that represents the composite at filament scale. This technique is compared to three-layers scale models and experimental measurements of the actuation for assessing the reliability of the in–house FE approach to explore the design space of hygromorphs. Moreover, this comparison would provide indications about the efficiency of the in–house FE technique to account for printing artefacts specific to the 4D printing of the PLA/continuous flax fibres filaments.

2. Materials and experimental methods

2.1. Filament production and printing of the hygromorph biocomposites

The filament used to make the hygromorph biocomposites (HBC) specimens was produced by forcing a continuous flax fibre yarn in a nozzle with flowing melted PLA. As a consequence, the filament used could not be cut during printing. For greater details please see a previous study on this subject [31]. The geometries studied were produced by compressing the filament on the printing surface. Each geometry printed with a custom modified Prusa i3 MK3S printer is presented in Figs. 1 and 2. The latter was adapted from the seminal calla lilly example developed by Gladman et al.'s work [11]. Details about the modifications of the 3D printer (i.e., the nozzle and the extrusion system) have been provided in a past study [31]. The samples produced are named angle HBC (aHBC), curvilinear HBC (cHBC) and calla lily HBC. The fibre paths of the different specimens were obtained by joining functions one after the other (i.e. linear for aHBC, quadratic for cHBC and calla lily HBC). In Fig. 1 a), Layer 1 is the active layer, that triggers the actuation. The active layer is characterised by a high coefficient of moisture expansion and low stiffness. Layers 2 and 3 are the passive components of the hygromorph (i.e., they possess high stiffness and low coefficient of moisture expansion). As shown in Fig. 1 b), circular specimens are investigated to explore the double curvature effect, while avoiding the effect provided by the corners upon actuation. This is similar to the specimens developed by Gladman et al. [11]).

2.2. Conditioning for hygromorphism

The calla lily, angle and cHBCs were first dried at 38°C for 6 h to remove the majority of the water from the specimens. The samples
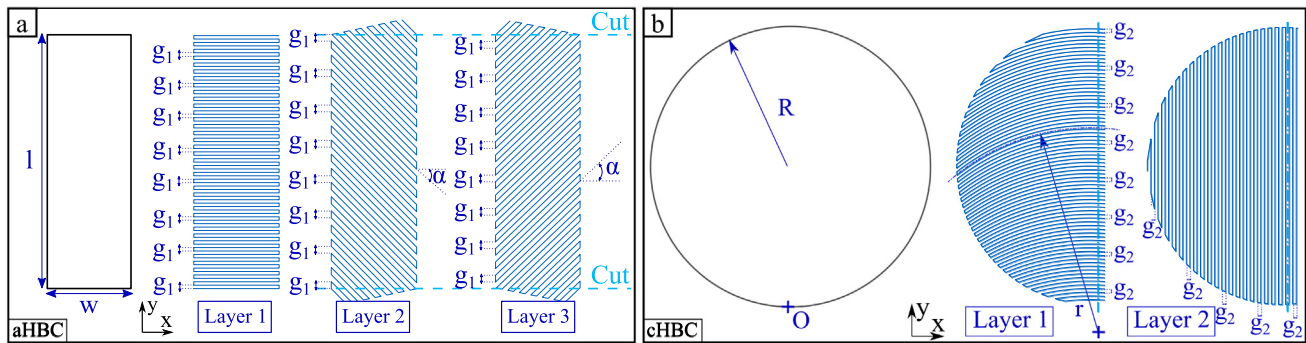
Fig. 1. (a): Geometry (left), printing pattern (right) for aHBC. Design variables: $\alpha \in \{0, 10, 30, 40, 45, 50, 60, 80\}°$: studied parameter with values selected to focus on the region of amplitude increase $\approx 45°$ (tilt angle of the passive layers- Layers 2 & 3), $g_1 = 0.8$ mm (distance between two filaments), w = 10 mm (width of the specimens), l = 60 mm (length of the specimens). (b): Geometry (left), printing pattern (right) for the cHBC. Printing variables: R = 30 mm (radius of the specimen), r$\in$\{30, 31, 40, 45, 50, 100\}mm: studied parameter (radius of curvature for Layer 1), g_2=0.8 mm (distance between filament).
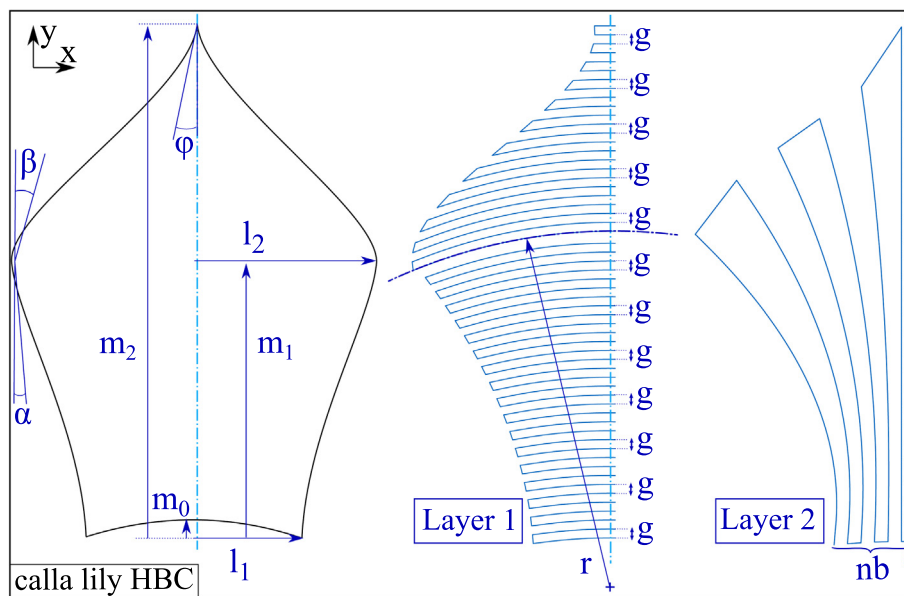

Fig. 2. Geometry (left) and printing pattern (right) of the structure mimicking the calla lily flower. Printing variables: $\alpha = 41°$ (tangent of the general geometry at its widest point in direction Y$^+$), β=0° (tangent of the general geometry at its widest point in direction Y$^-$), $\varphi = 0°$ (tangent of the highest point of the specimen), $m_0 = 1$ mm (distance between the lowest point and the highest point of the lower curvature), $m_1 = 70$ mm (distance between the lowest point and the height of the widest point of the specimen), $m_2 = 120$ mm (length of the specimen), $l_1 = 32$ mm, l_2=44 mm, g = 0.8 mm, nb = 19 (nb is the filament in the half layer), r = 60 mm.

were then conditioned in a box at 11% RH. These samples were then transferred to the 98% RH box to perform the actuation tests. This range of humidity was selected as the largest non immersed level achievable. The 98% and 11% RH values were obtained using glass Petri dishes filled with water mixed with potassium sulfate and with potassium hydroxide, respectively.

2.3. Evaluation of the actuation

2.3.1. Angle HBC (aHBC)

The set up and post-processing adopted to quantify the actuation of the aHBC is presented in Fig. 3. Fig. 3 a) shows that the aHBCs are laid down horizontally on top of the conditioning glass Petri dishes. Twelve target points (six on each side - see the black tracking points in Fig. 3 b)) are placed on the specimens to track their actuation. The light intensity was not varied during the experiment to limit its impact on the relative humidity inside the desiccator. An image was acquired every minute for the first 20 min, and then every 5 min until the 3000 min mark using an

Imetrum video gauge system. As presented in Fig. 3 c), The curvature is obtained from a least square interpolation calculated using a Python function. Average values between both sides are used to compare to the analytical and FEA models. The evolution of the curvature over a time span of 3000 min is defined as $\delta\kappa$ and was calculated between the curvature at dried state and the one after 3000 min (see Fig. 3 d)).

To evaluate the actuation reactivity (i.e., speed) in the aHBC, a spline interpolation was applied to the data using the python function *interpolate.splrep* (See Fig. 3). The spline interpolation function was then differentiated via the *interpolate.splder* Python function. The initial value of the differentiated function was used as the measure of the aHBC actuation reactivity.

2.3.2. Calla lily and curvilinear HBCs (cHBCs)

The actuation of the curvilinear and the calla lily HBCs specimens was measured via three-dimensional Digital Image Correlation (DIC) using a Davis Lavision 5 Mega pixel camera system [30]. The specimens are held vertically in a 98% RH conditioned
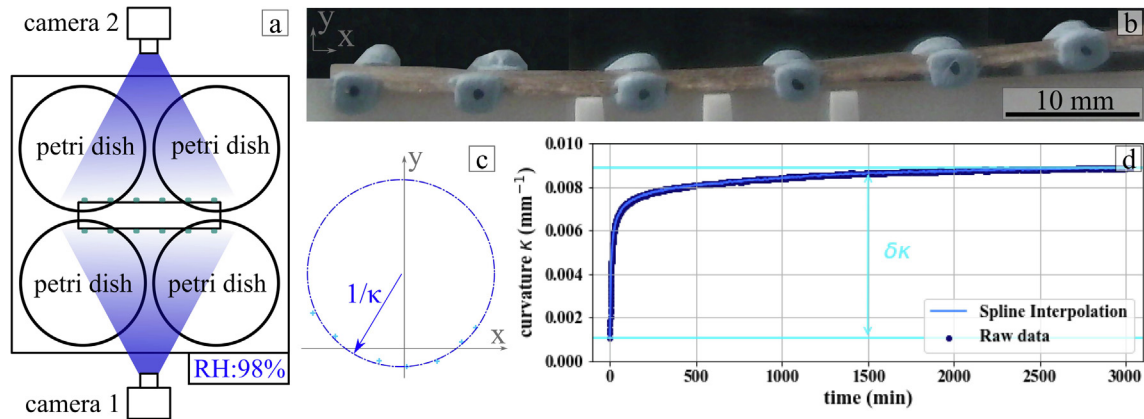
Fig. 3. (a): Schematic of the measurement set up. (b): Example of images taken by the video gauge. (c): Example of curvature measurement (d): Example of curvature evolution during a test.

glass box. The DIC records one image every 30 s for the two first hours, then one image every 5 min during a whole week. An example of the post-processing applied to the cHBC is presented in Fig. 4. An example of DIC image is presented in Fig. 4 a). The post-processing was performed with 29 pixels subset size and 9 pixels step size. The surface presenting the positions of the subsets in space was then smoothed with a four degrees polynomial interpolation (see Fig. 4 b)). The AoM presented in Fig. 4 c) highlight the axes used for the curvature measurements. The intersections of these lines with four circles (0 mm, 8 mm, 18 mm and 28 mm radius) are projected onto the deformed specimen. Seven points are therefore used to quantify the curvature for every AoM configuration. The measure of the curvature was made via a least square interpolation (see Fig. 4 d)). Fig. 4 e) presents the evolution of this curvature in time. To define the end of the experiments, the AoM at which the normalised curvature varies the most during the final hours of the test was considered (normalisation performed using the maximum curvature at each AoM). The time history of the normalised curvature was interpolated with a power function ($f(x) = a^*x^b + c$, $(a,b,c) \in \mathbb{R}^3$). The final position of the test corresponds to the time for which less than 5% of the actuation range interpolated via the power function is reached in less than 48 h. As presented in Fig. 4 f), the differences between initial and final curvatures ($\delta\kappa$) were compared against those obtained with the in–house FE model. A similar post-processing approach was applied to the calla lily HBC.

3. Models

The mechanical and hygro expansion properties used for the different layer scale models are presented in Table 1, respectively [13,30]. The properties listed are related to the measurement of the composite layers thickness (0.24 mm), as well as the evolution of the moisture content (5.77%) in the composites between 11% and 98% relative humidity [13]. In Table 1, the indices 1, 2 and 3 correspond to the direction parallel to the fibre (longitudinal), to the width direction (transverse) and the through-the-thickness direction (out-of-plane).
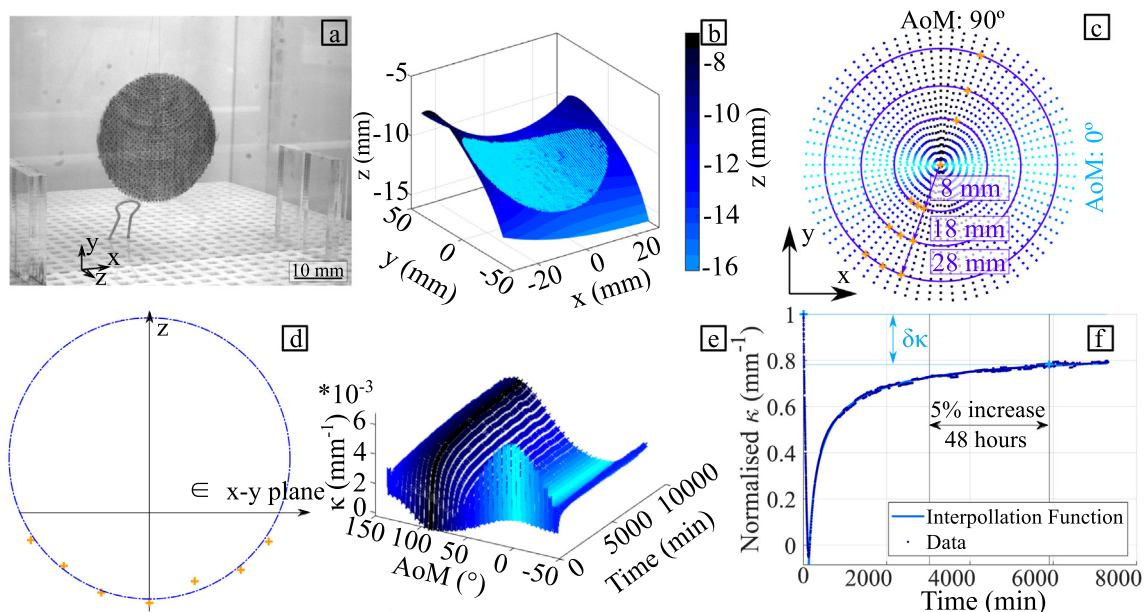

Fig. 4. (a): Example of DIC image. (b): Example of position in space of the DIC subsets. (c): The Angle of Measure (AoM) shown by the dashed lines (every 5° around the specimens) (d): Example of curvature calculation. (e): Surface plot showing the evolution of the curvature with the time for every AoM. (f):Example of $\delta\kappa$ calculation.

3.1. Timoshenko for aHBC

Timoshenko beam theory is a 1D model that includes a passive ($[\alpha°; -\alpha°]$) and an active layer $[90°]$ with low and high sensitivity to variation of the RH, respectively [32]. The Classical Laminate Theory (CLT) is used to obtain the equivalent orthotropic properties of the passive layer. Comprehensive description of the CLT can be found in Jones et al. [33]. The stiffness matrix for a lamina is used to obtain the *ABD* matrix of the passive layer (See Eq. 1). From this matrix, joining the curvatures and strains (κ and ϵ^0) to the loads (N and M) the equivalent properties of the passive layer can be obtained.

$$\begin{bmatrix} \epsilon^0 \\ \kappa \end{bmatrix} = \begin{bmatrix} A & B \\ B & D \end{bmatrix}^{-1} * \begin{bmatrix} N \\ M \end{bmatrix} \quad (1)$$

Eq. 2 is then used to determine the curvature evolution $\delta\kappa_x$ [32]. The small deformation assumption is not fully respected by the beam tested. Hence, the beam undergo plastic deformations. This artificially stiffens the Timoshenko beam model.

$$\delta\kappa_x = \frac{6 * \delta\beta * \delta MC * (1+t)^2}{(t_a + t_p) * (3 * (1+t)^2 + (1+t*e) * ((t)^2 + 1/t * 1/e))} \quad (2)$$

In Eq. 2, t=t_p/t_a (t_p and t_a are the thickness of the passive and active layer, respectively) and e=E_p/E_a (E_p is the longitudinal and E_a transverse stiffness for the passive and active layer, respectively). The term $\delta\beta$ is the difference of the coefficient of the moisture expansion between the two humidity levels at which the specimens undergo a δMC moisture content variation.

3.2. Finite Element Analysis

In all finite element models the hygroscopic actuation of the specimen was represented via the thermal expansion Abaqus toolbox with an isotropic conductivity of 34 mJ*(s*mm*K)$^{-1}$. The first two FEA approaches used to model the aHBCs differ by the types of elements implemented. One used 15000 classic shell (S4RT: inspired by Gigliotti et al.[34]) and the other 225000 3D elements (C3D20RT). The number of elements were selected for the in plane element size to be identical between the shell, the solid (aspect ratio of the elements: 4) and the in–house FE models. No mechanical boundary condition was imposed in the models. The positions of the seven nodes on the 60 mm long sides of the HBCs configurations are extracted from the model. These points are then post-processed identically to the ones from the tests (See Fig. 3). Each model was run for every integer angle ($\alpha°$) from 0° to 90°.

For both the aHBCs and cHBCs, an in–house FE model, inspired by the design of multi material actuators [35,36] was also implemented [30]. In this model, a.png image was obtained from the *matplotlib Python* plot representing the filament path used to create the gcode for the printing of the specimens. The image allowed evaluation of the fibre volume fraction and the fibre orientation of the composite at each pixel. The fibre volume fraction is obtained thanks to the grayscale on each pixel of the.png. The orientation of the fibre was obtained using the grayscale gradient of one pixel and its closest neighbours. The number of pixels, hence the resolution of the model, is tailored to the compaction of the filament printed. The more compacted the filament, the more pixels are

needed until the fibre path is too compacted to distinguish between filaments. Hence, the superposition of images was used to obtain voxel-like 3D distributions of fibre volume fraction and fibre orientation. These independently defined properties were turned into an FEA model (elements: S4RT). No boundary condition was applied to the aHBC model. For the cHBC, pinned boundary conditions were implemented on the node intersecting the edge and the symmetry axis of the specimen (point "O" in Fig. 1); this is representative of the string holding the sample during the test. After extracting the position of all the nodes from the FEA model, the same post-processing strategy used for the experimental tests was implemented (see Fig. 4). Unlike all the other models implemented (layer scale), the voxel-based one is defined at the filament scale. Hence, filament/fibre properties are used as input in the voxel-based model. These properties are provided in Table 2.

4. Results and discussion

4.1. Calla lily flower-shaped HBC

Fig. 5 shows examples of images recorded during the hygromorphism of the calla lily HBC. It also features the evolution of the curvatures measured along two perpendicular axes.

In Fig. 5 the initial responsiveness of the curvature in the longitudinal direction (κ_l=-1.7*10^{-2}mm^{-1}) is almost hundred times larger than along the transverse direction (κ_t=1.6*10^{-4}mm^{-1}). During the test, the absolute values of these two curvatures also increase quickly, reaching the values of 6.6*10^{-3}mm and 1.7*10^{-4}mm after 470 min for the transverse and longitudinal curvatures, respectively. Hence, at 470 min of experiment, κ_t is 40 times larger than κ_l. At the final actuation stage, the longitudinal curvature (κ_l=0.9*10^{-4}mm^{-1}) is almost 1.5 times lower than the transverse (κ_t=1.4*10^{-3}mm^{-1}). These values show the difficulty in generating large anticlastic double curvature from the proposed configuration of flax/fibre PLA printed composites. At the initial position and after 470 min of experiment, a large $\kappa \approx 10^{-2}$ actuation is evident in one of the two curvatures, while the other one is extremely low ($\kappa \approx 10^{-4}$). Only at the end of the test, the two curvatures show similar actuation ranges ($\kappa \approx 10^{-3}$). However, the actuation along the x and y directions are limited, compared to those achieved by Gladman et al. with cellulose fibril reinforced hydrogels and with similar printing patterns [11]. A larger actuation authority would be needed to mimic the morphing provided by the calla lily flower geometry at 98% RH.

As the Calla lily flower has a complex geometry, more diverse printed material distributions defining the mesostructure should be assessed for obtaining the anticlastic double curvature actuation, which is the objective the biomimicking exercise. The anisotropy, stiffness and printing path variability can explain the difference of deformation obtained between the Calla lily shape obtained by Gladman et al. ([11]) and those generated in this study. Accordingly, the influence of the curvature of the printing path on one layer was used to study the feasibility of anticlastic double curvature configurations. The strategy adopted is presented in Fig. 6. It starts by considering that the [0°;90°] stacking sequence only allows for a single curvature to be obtained. The Timoshenko curvature equation (See Eq. 2) for a bilayer material shows an increasing curvature if the stiffness of the passive layer

Table 1

Mechanical and hygroscopic properties implemented for the different models created [13] (E: stiffness, v: Poisson's ratio, G: Shear stiffness). β (Coefficient of Moisture Expansion), v_{23} and G_{23} were obtained in a previous study by the same authors [30].

E$_{11}$ (MPa)	E$_{22}$&E$_{33}$ (MPa)	v_{12}&v_{13}	v_{23}	G$_{12}$&G$_{13}$ (MPa)	G$_{23}$ (MPa)	β_{11}	β_{22}	β_{33}
6680	679	0.523	0.279	986	982.6	−0.0071	0.123	0.394

Table 2

E_{11} is obtained with the Rule of Mixture by considering v_f=0.3 and E_{PLA}=1.5GPa [13].The elastic constants E_{22}, E_{33}, G_{12}, G_{13}, v_{12} and v_{13} are calculated using the micro-mechanics equations provided by Cichocki et al. [37] and the properties from [30,38,39]. The terms β_{11} and β_{22}/β_{33} are obtained from de Kergariou et al. [30] and Le Duigou et al. [40]. v_{23} and G_{23} were obtained in a previous study by the same authors [30].

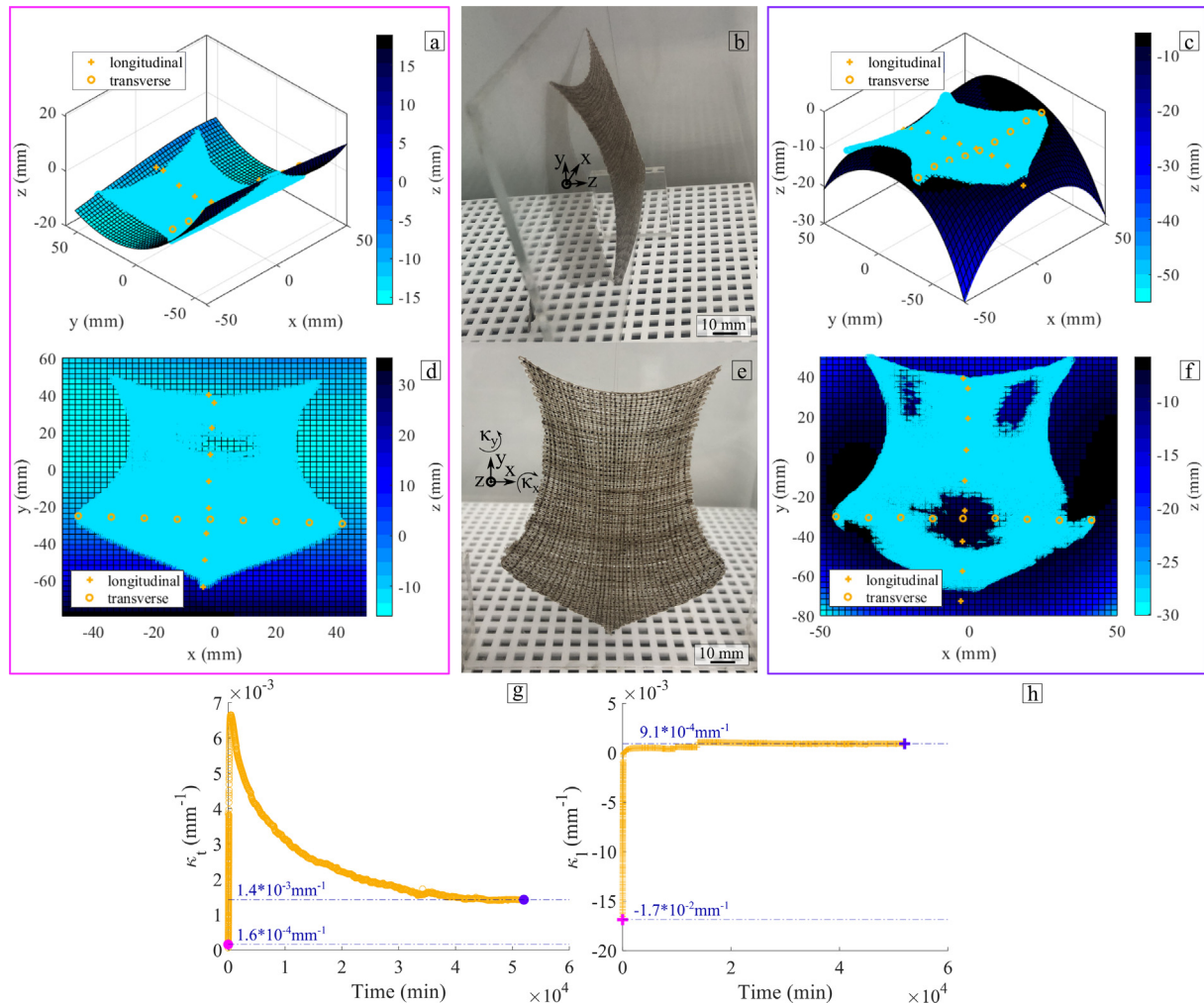| E_{11} (MPa)	E_{22} & E_{33} (MPa)	v_{12} & v_{13}	v_{23}	G_{12} & G_{13} (MPa)	G_{23} (MPa)	β_{11}	β_{22}&β_{33}
18997	414	0.0813	0.279	584	982.6	−0.0071	1.14

Fig. 5. Actuation of the calla lily hygromorph (a), (c), (d), (f): DIC points and interpolation. The points used to measure the curvature in the longitudinal (o) and transverse direction (x) are indicated in orange. a), d): Dried specimens (Time = 0 min in g) and h)). c), f): Specimen after conditioning (Time = 52020 min in g) and h)). b), e) isometric and top down views of the specimen during the recording of the actuation. The sign of the curvature presented are chosen arbitrarily. Specimens curvinge toward the support (see b)) are considered to present a positive curvature. g), h) Time histories of the transverse (κ_t) and longitudinal (κ_l) curvatures during conditioning.

(Layer 2 for κ_y) is reduced. Curving the filament of the passive layer allows for a reduction in the stiffness along the x direction when compared to the stiffness parallel to the filament. The Timoshenko equation is modified by now considering the stiffness of the bent filament layer (E_x), rather than the larger material stiffness (E_1).

The idea behind the aHBC evaluated here is similar to that of cHBC. The concept involves limiting the stiffness of the passive layer to allow for larger actuations. Here, tilting the angle of the passive layer from [0°;0°;90°] to [α°;-α°;90°] ($\alpha \in \mathbb{R}, \alpha \in [0°, 80°]$) is one of the strategies to achieve the reduction in the stiffness.

4.2. Curvilinear HBC (cHBC)

Fig. 7 presents the comparison of the evolution of the curvature between the FEA model and the tests conducted for every AoM

presented in Fig. 4. The figure also compares the maximum ($\delta\kappa_{max}$) and minimum ($\delta\kappa_{min}$) actuation obtained for the curvilinear specimens considered in this work. The minimum and maximum curvatures are obtained for 0° and 90° AoM, respectively. Fig. 7 a) shows the cosine-like shape of the $\delta\kappa$ versus the AoMs for both test specimens and FEA models. The $\delta\kappa_{min}$ of the test specimens is presented in Fig. 7 b), which decreases with the increase of the printing bend radius. The FEA models show the same order of magnitude of $\delta\kappa_{min}$ when compared with the test specimens. The numerical models present, however, a smaller decrease in $\delta\kappa_{min}$ ($1.1*10^{-3}$ mm^{-1}) when compared to the test specimens ($1.9*10^{-3}$ mm^{-1}). Similar conclusions can be also drawn for the $\delta\kappa_{max}$ value, which increases in the experimental specimens when larger printing bend radiuses are adopted ($7.9*10^{-3}$ mm^{-1}). The FEA model also shows this type of dependence, but to a smaller extend ($2.4*10^{-4}$ mm^{-1}). In terms of absolute curvatures, the larger the
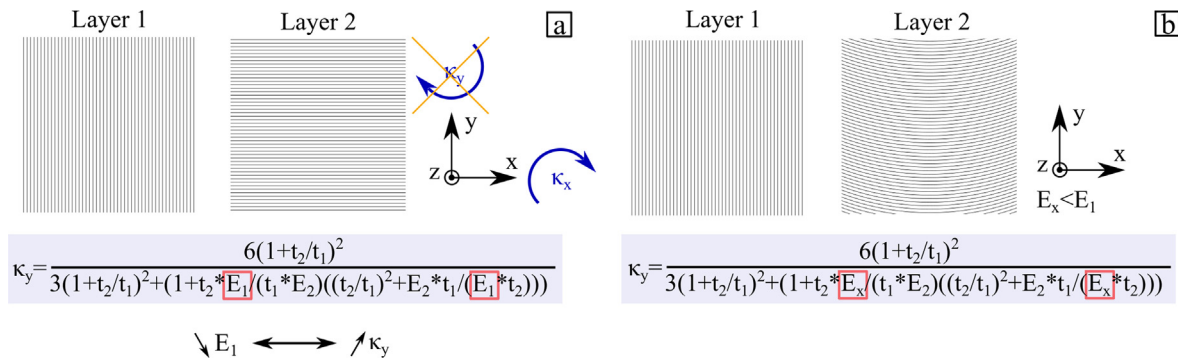
Fig. 6. The strategy adopted to obtain anticlastic curvature. (a): Timoshenko equation for cross ply composite. (b): Modification of the Timoshenko equation for cross ply composite with one layer whose filament was bent.
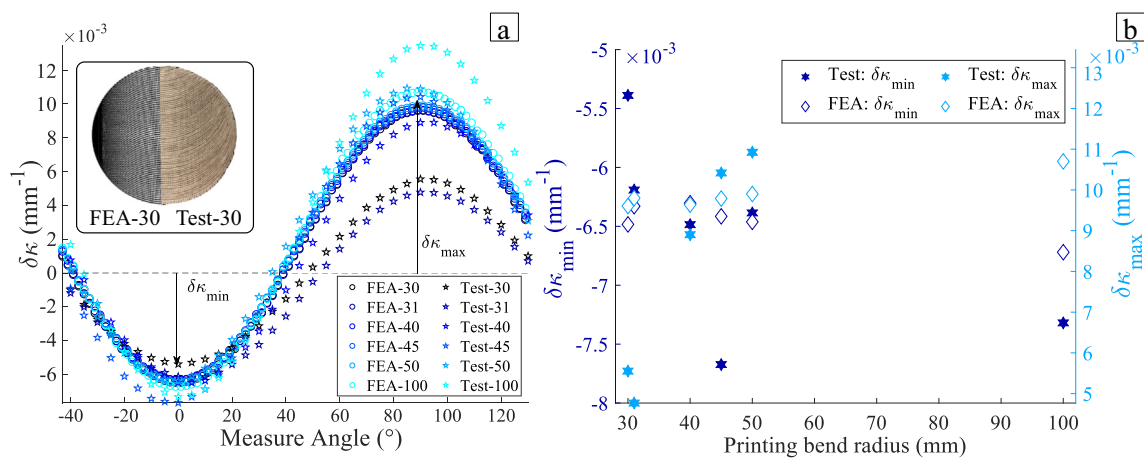

Fig. 7. Comparison between FEA and tests related to the cHBC designs: (a): Evolution of the curvature difference between the 11% RH and the 98% RH conditioned specimens for every AoM presented in Fig. 4. (b): Largest positive and negative curvature variations for every specimen (each with a different printing bend radius).

printing bend radius, the greater the actuation capability ($|\kappa_t|$ and $|\kappa_l|$). This evolution is also confirmed by the lower variations observed in the FEA models.

One of the reasons for the difference between FEA and experiments at low printing bend radius values of the $\delta\kappa_{max}$ is explained in Figs. 8 a), b). These Figures show the fibre orientation (quiver plot of every element of the FEM) in the case of the 30 mm printing bend radius. As the radius of the R = 30 mm specimen (see Fig. 1) becomes equal to the printing bend radius, an accumulation of the print path occurs at the edge of the configuration (turquoise square in Fig. 8 a)). The misaligned fibres shown in Fig. 8 b) are divided in two sections. In the first, ($y\in[27;28]$mm) the filaments represented by the grayscale in the G-code are starting to "fuse" together, preventing the Hessian matrix to track the black line representing every filament (see [30] for a description of the modelling technique). Hence, some arrows do not follow the global pattern of orientation as expected. In the second section ($y\in[28;29]$mm), the black lines representing the filaments are completely fused. Hence, the Hessian matrix calculation provides a null orientation by default, which is close to reality, but not the one expected at this location. For $y\in[28;29]$mm, the filament orientations are more directed along the x direction than they are in the printed specimens. The model therefore softens along the y direction and stiffens along the x one. This partial mismatch of filament directions in the model also provides some artificially high and low actuations along the y and x directions respectively (i.e., the fibres deform more transversely and not longitudinally). The $\delta\kappa_{max}$ is subsequently artificially lowered, whereas the $\delta\kappa_{min}$ is increased in the

in–house FE model. Such effect is observed for printing bend radii close to the specimen radius, in the present case it only appeared for the 30 and 31 mm bend radii. The other source of difference between the $\delta\kappa_{min}$ FEA and tests is due to the experimental set up. The numerical values of the $\delta\kappa_{min}$ are consistently larger than those arising from the experiments.

During the test, the timing between the opening of the desiccator used for the conditioning and the start of the DIC recording (including the setting up of the specimen in the box, closing the box and the launch of the recording) was as low as 20 s. Fig. 4 e) and f) show the presence of a fast actuation occurring at the initial 20s of the tests. During this rapid deformation, it is difficult to capture the full range of the actuation. Finally, the last source of difference between the model and the experimental values has been previously observed in a paper describing the modelling strategy [30]. In that study, the authors describe how the coefficient of moisture expansion (CME) was affected by the compaction and geometric distribution of the fibres. The CME used is a constant in the model and is measured from environmental scanning electron microscopy [40]. Hence, the CME was measured in a very different compaction configuration, compared to its use in the cHBC. Although the base distance between filaments is 0.8 mm (see g in Fig. 1), the bending of the filament reduces the distance between filaments at the bent edges and increases the compaction of the fibres, hence reducing the local CME. Furthermore, the in–house FE only models one layer at the time, whereas the CME value is obtained with no compaction. This artificially creates a source of error for the FEA model. Some assumptions of the model, such as the width
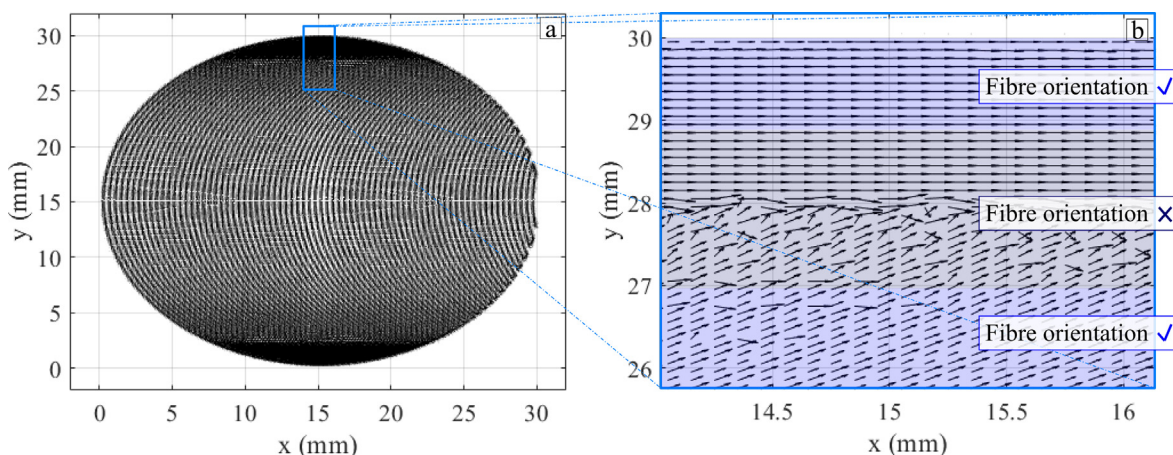
Fig. 8. (a) and (b) show zooms out and in of the fibre orientations considered in the FEA model for specimen with a printing bend radius of 30 mm. In the schematic, the blue background (Fibre orientation: √) and black background (Fibre orientation: ×) highlight the areas where the fibre orientation of the model fit and do not fit, respectively, to one printed on the specimens.
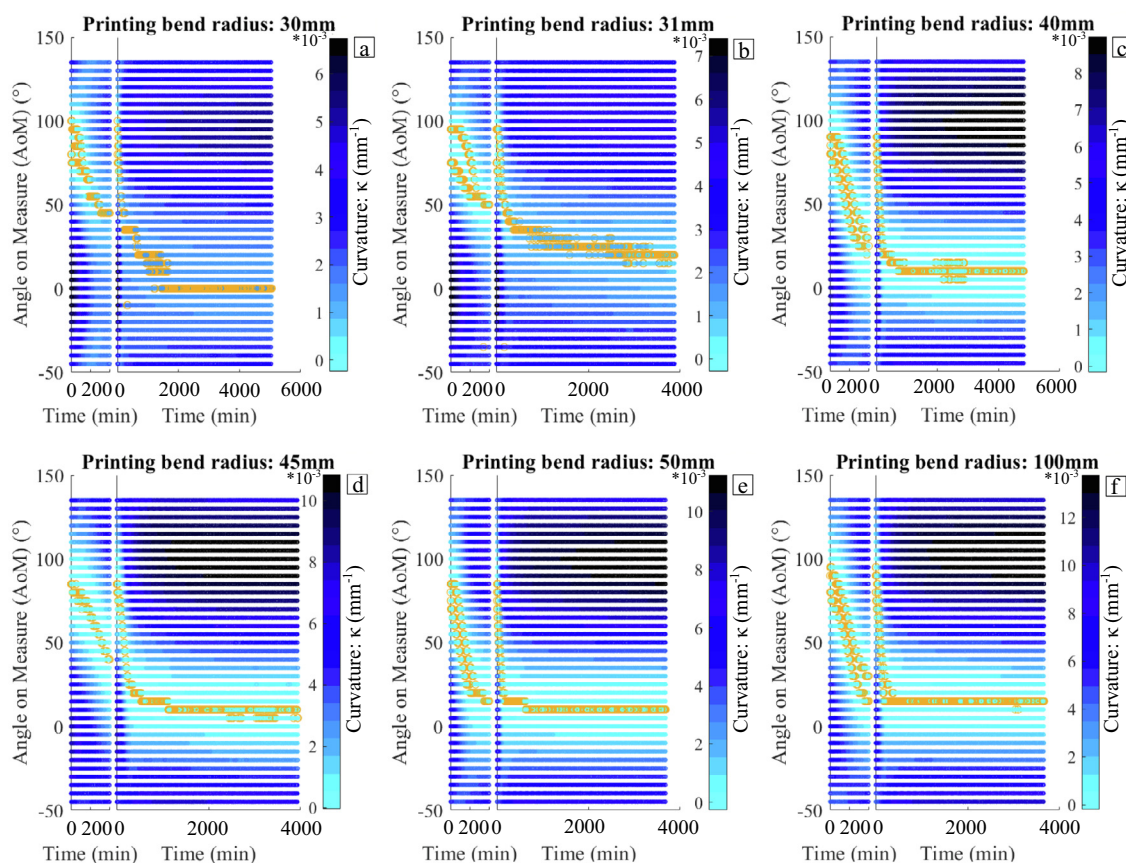

Fig. 9. Evolution of the curvature for all angles of measurement; printing bend radius: (a): 30 mm, (b): 31 mm, (c): 40 mm, (d): 45 mm, (e): 50 mm and (f): 100 mm. Top down view of the example image shown in Fig. 4 d). Each figure presents the entirety of the data used for the analysis (end criteria defined in Fig. 4 and a zoom in the first 200 min.

of the filament in the input image, also create differences between experimental and model results [30]. An example of an FEA model input and a printed specimen are presented together in Fig. 7 a). Despite obtaining a good approximation of the material distribution in the model, the filament width cannot be perfectly represented by the model.

Similarly to the case of the synclastic double curvature pine cone scale inspired composites made by Correa et al., it is neces-

sary to examine the curvature history for estimating the potential of the specimens to exhibit double anticlastic curvature [16]. Fig. 9 shows the curvature evolution for every value of AoM considered. The yellow circles in this figure indicate the transition between positive and negative curvatures (signs chosen arbitrarily: similar to Calla lily in Fig. 5) for every deformed specimen measured, or the minimum curvature at any given time if no null curvature values is found. The anticlastic double curvature actuation is pre-

sented with two distinct yellow lines at a given time. The distance between these two yellow lines gives the radial amplitude of one of the two curved parts of the target doubly curved geometry. The second part is presented by all the other AoMs. At a stable and asymptotic state (i.e., at the end of the test), all specimens show a single curvature actuation. The only anticlastic double curvatures highlighted here are observed during the first hundred minutes, and for a limited range of AoM values. The maximum AoM radial range of the anticlastic double curvature actuation between all specimens is 25°. This configuration with the maximum anticlastic double curvature actuation is obtained using a printing bend radius of 31 mm over 10 min of actuation, and it leads to a negative curvature close to $-3.0*10^{-4}mm^{-1}$. The negative curvature observed between the two yellow lines never exceeds $10^{-4}mm^{-1}$ in any specimen. Such actuation is negligible, compared to the rest of the curvatures observed. During the various phases of the experiment, the specimen is crossed by a neutral/flat axis (curvature: $\kappa \approx 0$ mm^{-1}). This neutral axis (yellow markers in Fig. 9) shifts from 90° to 0° AoM within the first 1000 min of the test. The shift of the actuation axis shows the possibility to controlling the speed of the bifurcation from initial to final shape via the radius of curvature of the curved layer. Fig. 9 shows that the radius of curvature affects the speed of the bifurcation. The greater responsiveness for larger radii of curvature of the printed curved layer is shown in Fig. 7. The shape of the specimen does not change with the bend radius (Example given in Fig. 4 b)), but the responsiveness of the actuation does. This responsiveness increases following an inverted exponential trend (See Fig. 4 f)).

4.3. Angle HBC (aHBC)

Fig. 10 shows the evolution of the curvature for all the aHBC specimens tested. Fig. 10 a) highlights the fact that most of the actuation occurs during the first 20 min of the conditioning independently of the α value. Fig. 10 b) also shows that a permanent (stationary) deformed state is reached after 3000 min in all the specimen tested. These two Figures also show that the variation of α does not contribute to the modification of the evolution of the curvature versus time. Hence, all the curves have been here interpolated with the same function to compute the actuation reactivity (graph of interpolation given in supplementary material).

Fig. 10 shows that it is possible to measure the speeds of the actuation for the different aHBCs. Those velocities are listed in Table 3. Table 3 demonstrates that the actuation speed increases

with the increase of the angle α, until it reaches 45°. The speed then decreases over the rest of the α range ([45°; 80°]). From Fig. 10, one could observe that the different specimens reach the final curvature at similar timings. Hence, the tailoring of the angle (α) cannot be used to create sequentially deforming structures [41,42]. Such tailoring is however interesting to use for generating synchronised deformations of the structure without the same actuation amplitude, as the speed will adapt to the shape the specimen must reach.

The measurement of the curvature actuation ($\delta\kappa$: Fig. 3) was performed after all the aHBC specimens have reached their permanent actuated state. The resulting values, as well as the values obtained with the Timoshenko equation and FEA models are presented in Fig. 11. Table 4 presents the difference between curvature actuation ($\delta\kappa$) from the measurements and models.

The models and the experimental values all show the same general trend, with symmetry versus the α=0° axis. From α=0°, the curvature actuation ($\delta\kappa$) increases with α to reach a global maximum (α_{max}) and then decreases to 0 mm^{-1} for α=90° (aHBC: [90°]$_3$, symmetric stacking sequence). These results are due to the presence of two competing mechanisms. The greater the value of α the stiffness of the passive layer, hence, the smaller the actuation becomes. However, the larger the value of α, the larger the expansion strain of the passive layer becomes and therefore, the greater the actuation. Two parameters are critical to quantify the increase of the actuation responsiveness in the hygromorph. The first is the *actuation maximizing angle*, i.e., the angle at which the global maximum actuation is obtained (dashed vertical lines). The second is the increase of actuation from the conventional HBC architecture [0°$_n$; 90°$_m$](where $n*m \in$ N^2), to the maximum value (vertical arrows); the latter is defined here as the *improved actuation potential*.

The maximum predicted actuation by the experimental, 3D solid-FEA, shell-FEA, Timoshenko and in–house FE model are obtained for α equal to 40°, 46°, 49°, 50° and 50°, respectively. The improved actuation potentials are $1.2*10^{-3}$ mm^{-1}, $2.0*10^{-3}$ mm^{-1}, $2.0*10^{-3}$ mm^{-1}, $6.6*10^{-3}$ mm^{-1} and $7.2*10^{-3}$ mm^{-1} for the 3D solid-FEA, shell-FEA, Timoshenko, in–house FE model and experimental, respectively. All the models and the experimental results confirm the possibility to increase the actuation of the HBC by having a passive layer made out of angle plies.

None of the models proposed was fully capable of predicting the actuation maximizing angle. The 3D solid-FEA, shell-FEA, Timoshenko and in–house FE model achieve gaps with the experiment as high as 6°, 9°, 10° and 10° difference with the actuation
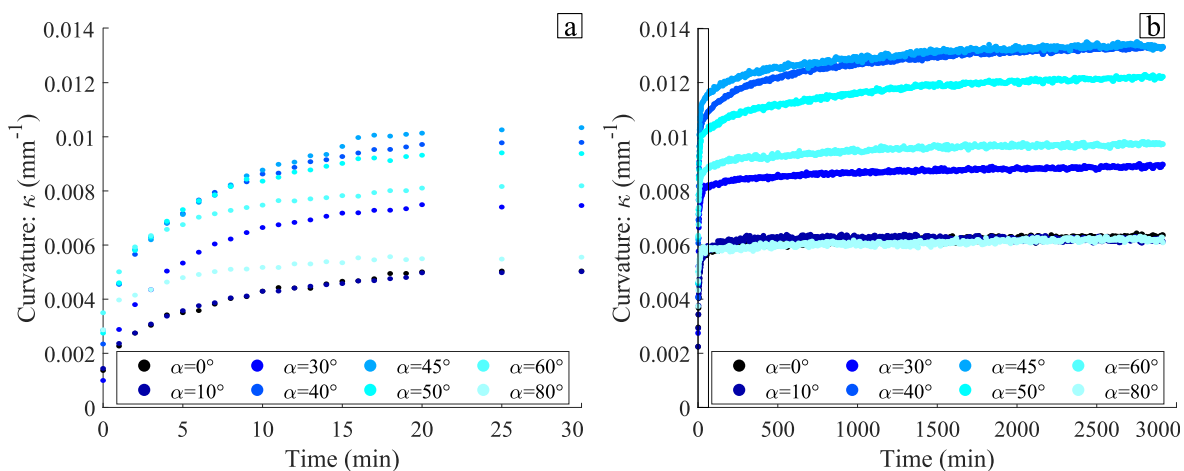

Fig. 10. Evolution of aHBCs curvature. (a): Time interval: [0; 30] minutes (b); Time interval: [0; 3000] minutes.

Table 3
Actuation speeds of all aHBC specimens tested.

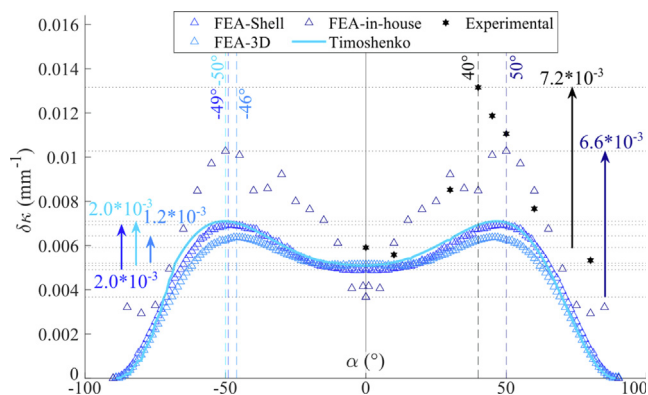| α(Fig. 1)	0°	10°	30°	40°	45°	50°	60°	80°
Speed $*10^4$ (mm*s)$^{-1}$	5.71	9.78	11.2	13.9	17.4	14.5	6.24	3.06

Fig. 11. Evolution of the curvature actuation ($\delta\kappa$, Fig. 3) with the orientation angle of the passive layer (α, Fig. 1). The vertical lines show the angle at which each model reaches the maximum curvature actuation (α_{max}). The horizontal intervals indicate the potential gain in actuation by changing the stacking sequence from [0°;0°;90°] to [α_{max}°;α_{max}°;90°].

maximizing angle obtained experimentally. Conversely, the in–house FE model was seen as the best technique to estimate the improved actuation potentials. It provides a relative discrepancy of 8.3% whereas the second best (the Timoshenko model) gives a value almost mine times as high (72.2%). Thanks to the values presented in Table 4, the in–house FE model was ranked as the best method to predict the experimental values. Fig. 11 shows that locally, other models are more efficient than the in–house FE model one (i.e. 3D solid-FEA, shell-FEA and Timoshenko for 0°). However, from Table 4 the average differences across the α values of $\delta\kappa_{Experimental}$ and $\delta\kappa_{FEA\_in-house}$, $\delta\kappa_{Timoshenko}$, $\delta\kappa_{FEA\_Shell}$ and $\delta\kappa_{FEA\_3D}$ are 0.0017 mm^{-1}±0.0014, 0.0031 mm^{-1}±0.0022, 0.0032 mm^{-1}±0.0021 and 0.0034 mm^{-1}±0.0023, respectively. Overall, the in–house FE model appears to offer the most precise design tool for hygromorphic structures similar to those presented here. One of the reasons for the difference between the models and the experimental results can be related to the assumption of static properties used for the model (i.e. all the models used constant material properties, although flax fibre reinforced PLA composites change with humidity [13]). All the models also consider materials without porosity, which does not accurately recapitulate the complex porous network in flax-PLAs [43]. It is known that porosity influences the actuation of hygromorphs [44].

One of the issues of the in–house FE model is its efficiency. For instance, the CPU time for aHBC is equal to 43.5 s for shell-FEA model and to 63.6 s for the in–house one. Hence, the in–house FE model is 32% slower than the shell-FE model. This is due to the discrete definition of the material properties of each element.

Consequently, this slowing effect will rise as the number of element increases. This limits the possibility to scale up the use of this modelling method. As a comparison, the calculation from the analytical model, Timoshenko, is almost instantaneous, and the 3D solid-FEA CPU time is 426.0 s.

An instability of the results is observed in the in–house FE model. For instance, the model for α=40° has a curvature lower than the ones at α=30° and α=35°, despite being in a part of the curve where the curvature is supposed to increase with α. Similar observations are made for α=80° and α=5°. These instabilities are for the most part due to the through-the-thickness alignment of the printing u-turns. As shown in Fig. 1, the aHBCs present u-turns along their edges (for greater details about these u-turns see [13]). These u-turns are positioned on the same *XY* plane locations (coordinates from Fig. 1) in the three layers for α=90°. As α decreases, the u-turn are no longer aligned, which creates additional through-the-thickness stresses. Fig. 12 b) presents the distribution of the von Mises stresses for the α=85° created by the asymmetry on the specimens. The largest stresses observed for this aHBC are generated by the asymmetry and are located at the edges of the specimens. Conversely, for lower α values (i.e.: 45° in Fig. 12 a)) all the filaments participate to the actuation, including the u-turns. As the angle continue to decrease, the u-turns tend to align and then misalign alternatively, until no u-turn related-stresses is present (α=0°). The in–house FE model appears to be the only technique capable of capturing the influence of the u-turn. Here its efficiency to predict experiment results is partially explained (see Table 4). However, some patterns are difficult to print with the technique used here, like those with tight acute angles [13]. As a consequence, the position and the dimensions of the u-turns printed will differ from those imparted by the parameters of the G-code used to produce the specimen, but also used as input in the in–house FE model. This also explains part of the difference between the experimental and in–house FE model results. The voxel-inspired models can account for printing artifacts such as u-turn. Hence, they can provide greater precision in the prediction of complex structures.

More reasons also lie behind the discrepancies between models and experimental results. The trackers (Fig. 3), positioned manually, are not perfectly aligned with the specimens. During the long period of times involved during the experiment and between measures, the temperature was not always constant which can lead to unwanted small humidity variations in the conditioning box. The resulting printed layers are also not necessarily homogeneous along the length of the specimen, as the filaments forming one layer are deposed one by one. Apart from the in–house FE model, none of the models here take into account the effect of the corners at the edges of the widths (Fig. 1).

Table 4
Difference of actuation between models and experiment for each value of α considered experimentally ($\delta\kappa_{Exp}$: $\delta\kappa_{Experimental}$). The curvature difference values are given in $*10^2$ (mm^{-1}).

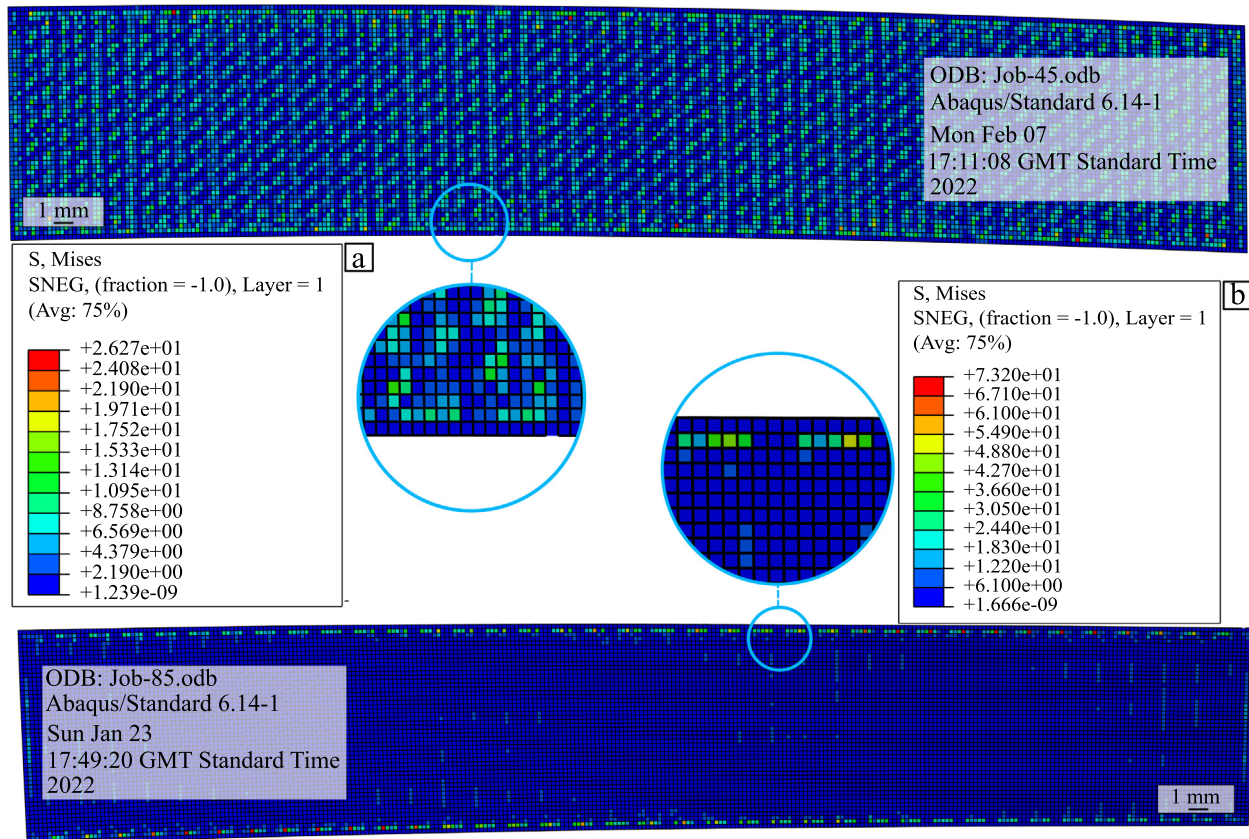| α(Fig. 1)	0°	10°	30°	40°	45°	50°	60°	80°
$\delta\kappa_{Exp}$	0.59	0.56	0.85	1.32	1.19	1.11	0.77	0.53
$\delta\kappa_{FEA\_in-house}$ - $\delta\kappa_{Exp}$	−0.22	0.05	0.07	−0.47	−0.18	−0.08	0.08	−0.24
$\delta\kappa_{Timoshenko}$ - $\delta\kappa_{Exp}$	−0.08	−0.04	−0.25	−0.64	−0.49	−0.4	−0.11	−0.45
$\delta\kappa_{FEA\_Shell}$ - $\delta\kappa_{Exp}$	−0.1	−0.06	−0.24	−0.64	−0.5	−0.42	−0.18	−0.42
$\delta\kappa_{FEA\_3Dsolid}$ - $\delta\kappa_{Exp}$	−0.08	−0.05	−0.29	−0.70	−0.55	−0.48	−0.21	−0.41

Fig. 12. Example of in–house FE model for the aHBC specimens, results presented are the von Mises stresses. (a) α = 45° (b) α = 85°.

5. Conclusion

This work has presented an exploration of the design space of 4D printed continuous flax fibres reinforced polylactic acid composites to be used in hygromorph actuations/shape changes at different relative humidity conditions. The work also contains the first attempt to develop a morphing and actuation structures that mimics the shape change of a calla lily flower using 3D printed continuous fibre and polymer filaments. Failing to do so resulted in the exploration of how to enhance the actuation of the hygromorph biocomposite (HBC) by testing the performance of [-α°,α°,90°] stacking sequences HBCs with a varying value of α. The potential to obtain double anticlastic curvature actuation via curving the filament of one layer in the [0°, 90°] HBCs has been also considered. Several conclusions can be drawn from this work:

- The calla lily shape hygromorphism could not be obtained with the implemented printed pattern from Gladman et al. [11]. This was due to the small actuation responsiveness, and the difficulty for both printed structures to display anticlastic double curvature characteristics.
- The study of [α°; -α°; 90°] (α=∈[0°; 80°]) HBCs has shown that the actuation amplitude can be increased by tailoring the angle α. When considering α=40° the amplitude is increased by 0.0072 mm^{-1} compared to the classical cross-ply hygromorph: [0°; 0°; 90°]. This is due to the stiffness reduction of the passive layer when its ply orientation goes from [0°]$_2$ to [40°]$_2$.
- The fastest actuation achievable is obtained when α=45°. The actuation speed increases from α=0° to α=45° and then decreases from α=45° to α=80°.

- In–house FE model was the best model to predict the actuation authority of α-dependent HBCs, followed by Timoshenko, shell-FEA and 3D solid-FEA. None of those models provide a precise estimation of the angle at which the actuation is maximal, the 3D solid-FEA, shell-FEA, Timoshenko and the in–house FE model displayed a 6°, 9°, 10° and 10° gaps with the experimental work, respectively. The in–house FE model approximated the responsiveness of the actuation improvement peak with a 8.3% error gap.
- Bending the printing filament of a [0°;90°] hygromorph was described as an inefficient way to obtain anticlastic double curvature with continuous flax fibre PLA composites. The shift of the actuation direction during conditioning shows the bifurcation actuation possibilities for such geometry. Bending the printing filament from a 100 mm to a 30 mm bending radius modified the curvature obtained from 1.9*10^{-3}mm^{-1} to 7.9*10^{-3}mm^{-1} depending on the position on the specimen. Hence, it could be utilised to control the amplitude of actuation.
- The in–house model appears to be effective in predicting the behaviours of cHBC specimens, as long as the filaments used for printing are not too compacted. The model loses track of the fibre orientation if neighbouring print paths are too close to each other.

6. Data Availability

One example of Abaqus input file (.inp) for each FEA model presented in this study are made available at: https://data.bris.ac.uk/data/dataset/32jmyo2uldn312pdoa53a0ro28. Any other research (i.e..inp with exact mesh size presented) related data will be made available on request.

Declaration of Competing Interest

The authors declare that they have no known competing financial interests or personal relationships that could have appeared to influence the work reported in this paper.

Acknowledgement

Appendix A. Supplementary material

Supplementary data associated with this article can be found, in the online version, at https://doi.org/10.1016/j.matdes.2022.111472.

References

[1] E.A. Peraza-Hernandez, D.J. Hartl, R.J. Malak, D.C. Lagoudas, Origami-inspired active structures: A synthesis and review, Smart Mater. Struct. 23 (9) (2014) 28.

[2] M. Rüggeberg, I. Burgert, Bio-Inspired wooden actuators for large scale applications, PLoS ONE 10 (4) (2015) 1–16.

[3] A. Holstov, B. Bridgens, G. Farmer, "Hygromorphic materials for sustainable responsive architecture," Constr. Build. Mater., vol. 98, pp. 570–582, 11 2015.

[4] A. Le Duigou, G. Chabaud, F. Scarpa, M. Castro, Bioinspired Electro-Thermo-Hygro Reversible Shape-Changing Materials by 4D Printing, Adv. Funct. Mater. 29 (40) (2019) 1–10.

[5] Q. Wang, X. Tian, L. Huang, D. Li, A.V. Malakhov, and A.N. Polilov, "Programmable morphing composites with embedded continuous fibers by 4D printing," Mater Des, vol. 155, pp. 404–413, 10 2018.

[6] A. Le Duigou, V. Keryvin, J. Beaugrand, M. Pernes, F. Scarpa, M. Castro, Humidity responsive actuation of bioinspired hygromorph biocomposites (HBC) for adaptive structures, Compos. Part A Appl. Sci. Manuf. 116 (2019) 36–45.

[7] M.M. Lu, C.A. Fuentes, A.W. Van Vuure, "Moisture sorption and swelling of flax fibre and flax fibre composites," Compos. B Eng., vol. 231, pp. 1–10, 2 2022.

[8] S. Réquilé, A. Le Duigou, A. Bourmaud, C. Baley, "Deeper insights into the moisture-induced hygroscopic and mechanical properties of hemp reinforced biocomposites," Compos. Part A Appl. Sci. Manuf., vol. 123, pp. 278–285, 8 2019.

[9] A. Le Duigou, S. Requile, J. Beaugrand, F. Scarpa, M. Castro, "Natural fibres actuators for smart bio-inspired hygromorph biocomposites," Smart Mater. Struct., vol. 26, pp. 1–12, 12 2017.

[10] A. Bourmaud, J. Beaugrand, D.U. Shah, V. Placet, C. Baley, Towards the design of high-performance plant fibre composites, Prog. Mater. Sci. 97 (2018) 347–408.

[11] A. Sydney Gladman, E.A. Matsumoto, R.G. Nuzzo, L. Mahadevan, J.A. Lewis, Biomimetic 4D printing, Nat. Mater. 15 (4) (2016) 413–418.

[12] V. Mazzanti, L. Malagutti, and F. Mollica, "FDM 3D Printing of Polymers Containing Natural Fillers: A Review of their Mechanical Properties," Polymers, vol. 11, p. 1094, 6 2019.

[13] C. de Kergariou, H. Saidani-Scott, A. Perriman, F. Scarpa, A. Le Duigou, "The influence of the humidity on the mechanical properties of 3D printed continuous flax fibre reinforced poly(lactic acid) composites," Compos. Part A Appl. Sci. Manuf., vol. 155, pp. 1–12, 4 2022.

[14] L. Ren, B. Li, K. Wang, X. Zhou, Z. Song, L. Ren, and Q. Liu, "Plant-Morphing Strategies and Plant-Inspired Soft Actuators Fabricated by Biomimetic Four-Dimensional Printing: A Review," Front. Mater., vol. 8, p. 90, 5 2021.

[15] E. Reyssat, L. Mahadevan, "Hygromorphs: from pine cones to biomimetic bilayers," J.R. Soc. Interface 6 (2009) 951–957.

[16] D. Correa, S. Poppinga, M.D. Mylo, A.S. Westermeier, B. Bruchmann, A. Menges, T. Speck, "4D pine scale: biomimetic 4D printed autonomous scale and flap structures capable of multi-phase movement," Phil. Trans. R. Soc. A, vol. 378, pp. 1–18, 3 2020.

[17] P. Li, L. Pan, D. Liu, Y. Tao, S.Q. Shi, "A Bio-Hygromorph Fabricated with Fish Swim Bladder Hydrogel and Wood Flour-Filled Polylactic Acid Scaffold by 3D Printing," Materials 2019, Vol. 12, Page 2896, vol. 12, p. 2896, 9 2019.

[18] S. Zeng, Y. Gao, Y. Feng, H. Zheng, H. Qiu, J. Tan, Programming the deformation of a temperature-driven bilayer structure in 4D printing, Smart Mater. Struct. 28 (105031) (2019) 1–13.

[19] O. Testoni, T. Lumpe, J.-L. Huang, M. Wagner, S. Bodkhe, Z. Zhakypov, R. Spolenak, J. Paik, P. Ermanni, L. Muñoz, K. Shea, A 4D printed active compliant hinge for potential space applications using shape memory alloys and polymers, Smart Mater. Struct. 30 (085004) (2021) 1–12.

[20] M. Bodaghi, A.R. Damanpack, and W.H. Liao, "Self-expanding/shrinking structures by 4D printing," Smart Mater. Struct., vol. 25, p. 105034, 9 2016.

[21] S. Poppinga, M. Joyeux, Different mechanics of snap-trapping in the two closely related carnivorous plants Dionaea muscipula and Aldrovanda vesiculosa, Phys. Rev. E 84 (4) (2011) 1–7.

[22] F.J. Esser, P. Auth, and T. Speck, "Artificial Venus Flytraps: A Research Review and Outlook on Their Importance for Novel Bioinspired Materials Systems," Front. Rob. AI, vol. 7, pp. 1–13, 7 2020.

[23] J. Schmied, H. Le Ferrand, P. Ermanni, A.R. Studart, A.F. Arrieta, Programmable snapping composites with bio-inspired architecture, Bioinspir. Biomim. 12 (026012) (2017) 1–11.

[24] G. Sossou, F. Demoly, H. Belkebir, H.J. Qi, S. Gomes, and G. Montavon, "Design for 4D printing: Modeling and computation of smart materials distributions," Mater. Des., vol. 181, p. 108074, 11 2019.

[25] Y. Wang, X. Li, An accurate finite element approach for programming 4D-printed self-morphing structures produced by fused deposition modeling, Mech. Mater. 151 (2020) 12.

[26] Y. Wang and X. Li, "4D-printed bi-material composite laminate for manufacturing reversible shape-change structures," Compos. B Eng., vol. 219, p. 108918, 8 2021.

[27] K.G. Webber, D.P. Hopkinson, C.S. Lynch, Application of a Classical Lamination Theory Model to the Design of Piezoelectric Composite Unimorph Actuators, J. Intell. Mater. Syst. Struct. 17 (2006) 29–34.

[28] J.R. Kubalak, A.L. Wicks, C.B. Williams, M. Asme, Investigation of Parameter Spaces for Topology Optimization With Three-Dimensional Orientation Fields for Multi-Axis Additive Manufacturing, J. Mech. Des. 143 (5) (2021) 1–15.

[29] J.R. Kubalak, A.L. Wicks, C.B. Williams, Deposition path planning for material extrusion using specified orientation fields, Procedia Manuf. 34 (2019) 1.

[30] C. de Kergariou, B.C. Kim, A. Perriman, A. Le Duigou, S. Guessasma, and F. Scarpa, "Design of 3D and 4D printed continuous fibre composites via an evolutionary algorithm and voxel-based Finite Elements: Application to natural fibre hygromorphs," Addit. Manuf., vol. 59, p. 103144, 11 2022.

[31] A. Le Duigou, A. Barbé, E. Guillou, and M. Castro, "3D printing of continuous flax fibre reinforced biocomposites for structural applications," Mater. Des., vol. 180, pp. 1–8, 10 2019.

[32] B.Y.S. Timoshenko, Analysis of bi-metal thermostats, J. Opt. Soc. Am. 11 (3) (1925) 233–255.

[33] R.M. Jones, Mech. Compos. Mater., 7, CRC Press, 1998.

[34] M. Gigliotti, M.R. Wisnom, and K.D. Potter, "Loss of bifurcation and multiple shapes of thin [0/90] unsymmetric composite plates subject to thermal stress," Compos. Sci. Technol., vol. 64, pp. 109–128, 1 2004.

[35] C.M. Hamel, D.J. Roach, K.N. Long, F. Demoly, M.L. Dunn, H.J. Qi, Machine-learning based design of active composite structures for 4D printing, Smart. Mater. Struct. 28 (6) (2019) 1–11.

[36] Y. Wei, P. Huang, Z. Li, P. Wang, X. Feng, Design of active materials distributions for four-dimensional printing based on multi-material topology optimization, Smart. Mater. Struct. 30 (2021) 095002–095014.

[37] F.R. Cichocki and J.L. Thomason, "Thermoelastic anisotropy of a natural fiber," Compos. Sci. Technol., vol. 62, pp. 669–678, 4 2002.

[38] V. Harshitha, S.S. Rao, Design and analysis of ISO standard bolt and nut in FDM 3D printer using PLA and ABS materials, Mater. Today Proc. 19 (2019) 583–588.

[39] S. Farah, D.G. Anderson, and R. Langer, "Physical and mechanical properties of PLA, and their functions in widespread applications — A comprehensive review," Adv. Drug. Deliv. Rev., vol. 107, pp. 367–392, 12 2016.

[40] A. le Duigou, J. Merotte, A. Bourmaud, P. Davies, K. Belhouli, C. Baley, Hygroscopic expansion: A key point to describe natural fibre/polymer matrix interface bond strength, Compos. Sci. Technol. 151 (2017) 228–233.

[41] Y. Mao, K. Yu, M.S. Isakov, J. Wu, M.L. Dunn, and H. Jerry Qi, "Sequential Self-Folding Structures by 3D Printed Digital Shape Memory Polymers," Sci. Rep., vol. 5, p. 12, 9 2015.

[42] Y. Tahouni, F. Krüger, S. Poppinga, D. Wood, M. Pfaff, J. Rühe, T. Speck, A. Menges, Programming sequential motion steps in 4D-printed hygromorphs by architected mesostructure and differential hygro-responsiveness, Bioinspir. Biomim. 16 (2021) 7.

[43] C. Kergariou, A.L. Duigou, V. Popineau, V. Gager, A. Kervoelen, A. Perriman, H. Saidani-Scott, G. Allegri, T.H. Panzera, F. Scarpa, "Measure of porosity in flax fibres reinforced polylactic acid biocomposites," Compos. Part A Appl. Sci. Manuf., vol. 141, pp. 106183–106193, 11 2021.

[44] A. Le Duigou, D. Correa, M. Ueda, R. Matsuzaki, and M. Castro, "A review of 3D and 4D printing of natural fibre biocomposites," Mater. Des., vol. 194, pp. 1–26, 9 2020.